Supplementary Information

Forming and Compliance-free Operation of Low-power, Fast-switching HfO_xS_y/HfS_2 Heterostructure Memristors

Aferdita Xhameni[1,2], AbdulAziz AlMutairi[1,3], Xuyun Guo[4], Irina Chircă[3], Tianyi Wen[2], Stephan Hofmann[3], Valeria Nicolosi[4], and Antonio Lombardo[1,2*]

[1]London Centre for Nanotechnology, 19 Gordon St, London, WC1H 0AH, United Kingdom
[2]Department of Electronic & Electrical Engineering, Malet Place, University College London, WC1E 7JE, United Kingdom
[3]Department of Engineering, University of Cambridge, Cambridge CB3 0FA, United Kingdom
[4]School of Chemistry, Centre for Research on Adaptive Nanostructures and Nanodevices (CRANN) & Advanced Materials Bio-Engineering Research Centre (AMBER), Trinity College Dublin, Dublin 2, Ireland
[*]Corresponding author: Antonio Lombardo (email: a.lombardo@ucl.ac.uk)

1 Spectroscopic Imaging Ellipsometry

Figures 1a-b show the characteristic increase in transparency of a HfS_2 flake due to thermal oxidation. AFM images (c) were taken to determine flake thickness and surface roughness after oxidation (SI). A surface roughness of 125pm was determined in line with other work on the oxidation of HfS_2 [1,2].

Spectroscopic imaging ellipsometry (SIE) was employed for the high-resolution imaging and characterisation of partially and fully oxidised HfS_2 samples, measured in ambient conditions at room temperature. Each map pixel encodes a complete set of (Ψ, Δ) ellipsometric angles, which was fitted to a $HfO_xS_y/HfS_2/SiO_2/Si$ optical model[3] using the EP4Model software. The thickness information was extracted for each layer as 3D maps (Fig. 1d, e). The HfO_xS_y map shown in Fig. 1d confirms uniform oxidation across the entirety of the flake within the instrument resolution. No binning (defined as integrating N x N pixels of the original image into one pixel of the processed image) was applied during the data acquisition or image processing steps in order to maximise resolution, resulting in regions with signal loss (white pixels within the flake boundary). The complementary HfS_2 map from Fig. 1e demonstrates thicker regions still have some remaining HfS_2 signal, implying an oxide penetration depth of ∼4nm. In figures 1f-g we show the linescans 1 and 2 from figures 1c-e. The data contained shows the height measured by AFM and the SIE-derived HfO_xS_y and HfS_2 height profiles. At every point, the total sum of HfO_xS_y and HfS_2 thickness matches almost perfectly with the measured thickness of the flake estimated from AFM scans (Fig. 1c). The observed discrepancies in measured flake height from AFM and ellipsometry measured thicknesses (Fig. 1f-g) could originate from measurement noise, surface roughness and contamination, or discrepancy between the modelled oxide properties and

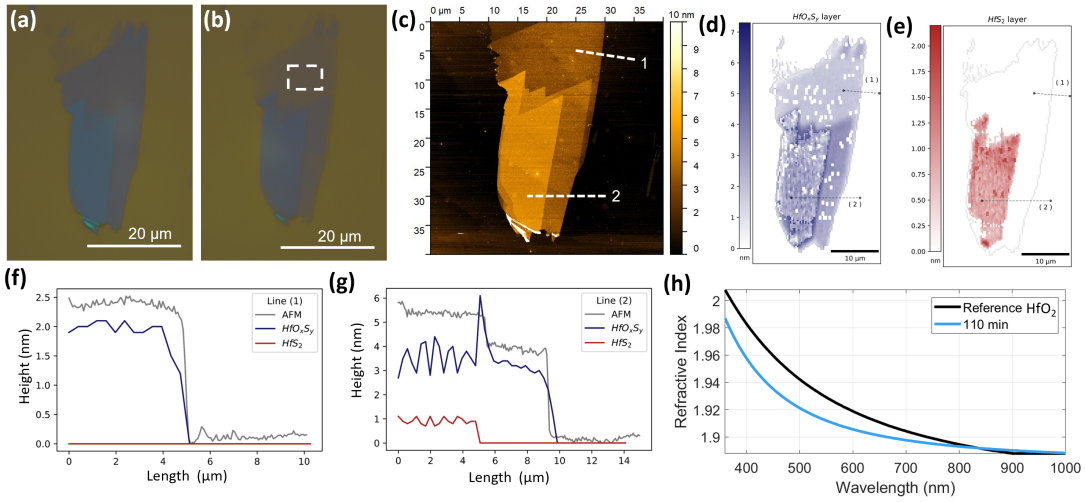

Figure 1: (a) HfS_2 flake prior to oxidation shows a blue colour, with opacity dependent on layer thickness of the material. (b) Post 110 min dry oxidation, oxidised material appears semi-transparent. The slightly brighter circle at the centre of the images is a microscope artifact and not a feature of the material. The boxed region indicates the region where the surface roughness was calculated by AFM (c). (d) SIE confirms that oxidation is uniform across the flake within the resolution of the instrument and that (e) thicker regions retain HfS_2. (f-g) AFM and SIE thickness profiles of the HfO_xS_y and HfS_2 linescans from figures c-e show that thicker regions retain HfS_2, whereas thinner regions are fully oxidised with an oxidation depth of ∼4nm. (h) Refractive index comparison between the 110 minute dry-oxidised flakes and a reference HfO_2 sample shows that a good agreement of the optical properties to a reference value can be achieved.

the measured sample. Between 5-9μm in Fig. 1g, we see that for regions of the flake less than or equal to ∼4nm thick, the flake is completely oxidised as no sulfide is present in the ellipsometry signal. For thicker regions, such as the region between 0-5μm in Fig. 1g, we see the remainder of the flake height is filled by unoxidised HfS_2. The increased oxide thickness observed along the flake edge is disregarded as a common SIE measurement artefact, as supported by AFM.

The complex refractive indices of the as-grown HfO_xS_y samples were extracted from the measured ellipsometric spectra, and were fitted using the Cauchy dispersion model, assuming a transparent dielectric layer in the probing wavelength range. The results were compared to the optical properties of HfO_2 as given on the publicly available SOPRA database[4] (Fig. 1h), showing a close agreement for the 110 minute dry oxidation recipe used in our devices.

2 Out-of-plane defects

We have observed out of plane defect paths in our 2D layered materials used for memristive devices described in the paper (Fig. 2). In-plane defect paths such as grain boundaries bridging electrodes have been observed by Sangwan et al[5]. They found that vacancies migrating withing the grain boundary could result in resistive switching due to the aggregation of charged defects

under applied field. Similar to other devices[6 7], this would lead to a modification of the Schottky barrier height (SBH)[5 8], showing very similar IV sweep behaviour to our devices, although we do not observe Schottky emission as a transport mechanism in the HRS or LRS. Out-of-plane defect paths have been shown to enable memristive switching by the same vacancy migration mechanism and have also been observed in multi-layered 2D layered materials such as hBN[9 10].

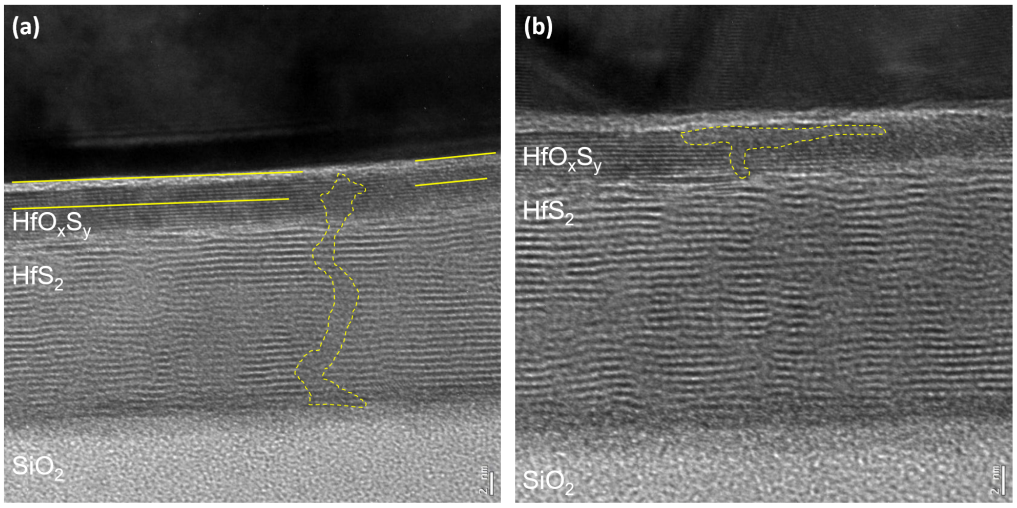

Figure 2: Out-of-plane defect paths in 110-minute oxidised HfO_xS_y/ HfS_2 structure can occur (a) throughout the flake and (b) within the oxide.

3 Pulsed Measurements

The pulse times for different waveforms generated by the waveform generator fast-measurement unit (WGFMU) integrated in the Keysight B1500 parameter analyzer with remote sensing units were examined under a 1GHz Keysight p9243a oscilloscope (Fig. 3a,b). The oscilloscope was connected to a remote sensing unit on the voltage input terminal of the memristor.

Generally, the pulse times were true to the pulse program sent from the WGFMU in total pulse width, however the pulse shapes were not square as they were programmed. WRITE and ERASE characteristics were examined (Fig. 3c,d) and we found that - much like other papers on fast-switching 2D materials-based memristors[11], the RESET occurs within the first part of the ERASE pulse. The latter part likely predominantly contributes to Joule heating, and is exhibited in all pulses that are long enough to contain the full extent of the ∼80ns RESET peak seen in the first portion of the WRITE and ERASE pulses. Finally we show a representative pulsed switching cycle obtained by 60ns, $\sim \pm 1$V pulses (Fig. 3e) on the devices showcased in the main text. The characteristics shown are largely similar between all the fast pulsed switching programs investigated. Recorded currents and energy consumption from 60ns switching (within the 80ns RESET threshold) are even lower than the other pulsing schemes investigated. Therefore, shorter timescales with dedicated sub-nanosecond pulsed switching units should be investigated

further.

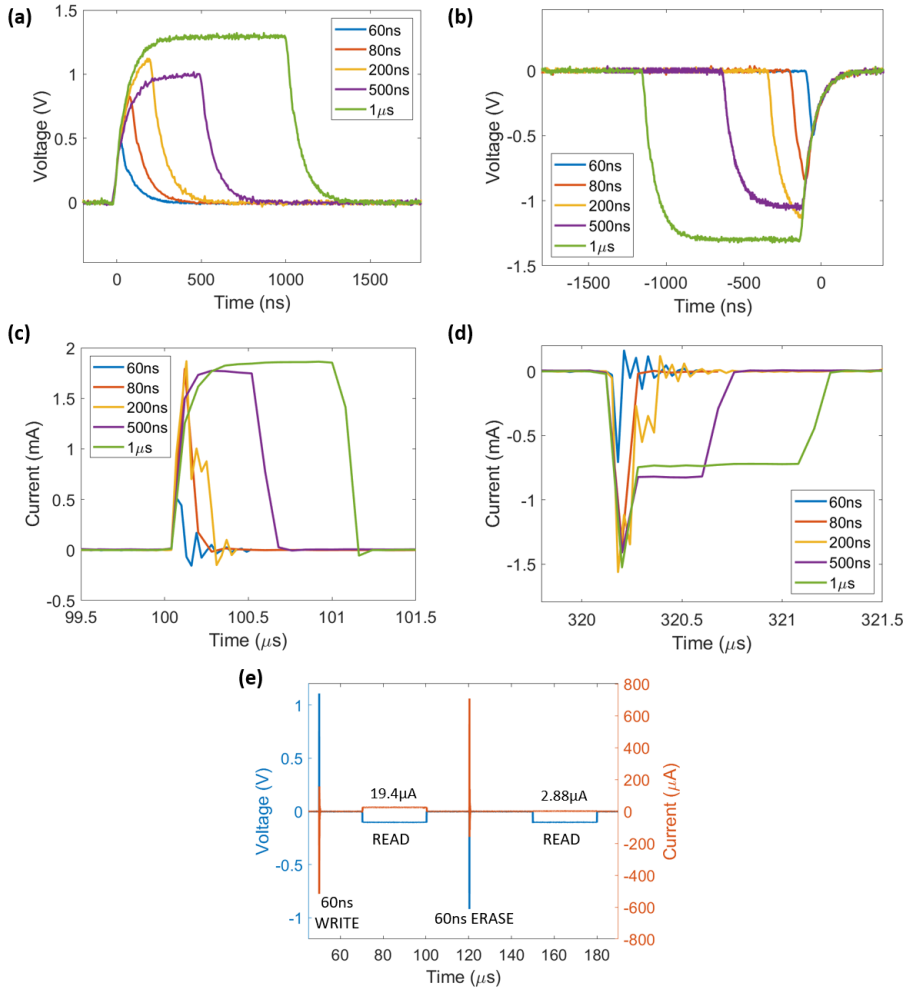

Figure 3: With the use of an oscilloscope, WRITE (a) and ERASE (b) input voltage waveforms used to switch devices were investigated in high time resolution. By looking at current vs time on a parameter analyzer, we can see that a significant portion of the resistive switching occurs in the first 80ns for both WRITE (c) and ERASE (d). Resistive switching has been demonstrated down to 60ns (e) with comparable characteristics to other pulsing schemes, but lower energy.

4 TCAD Simulations

A suite of simulations with sequential modifications made to the memristor materials stack to elucidate the role of each layer used in our Sentaurus TCAD simulations (Synopsys, 2022).

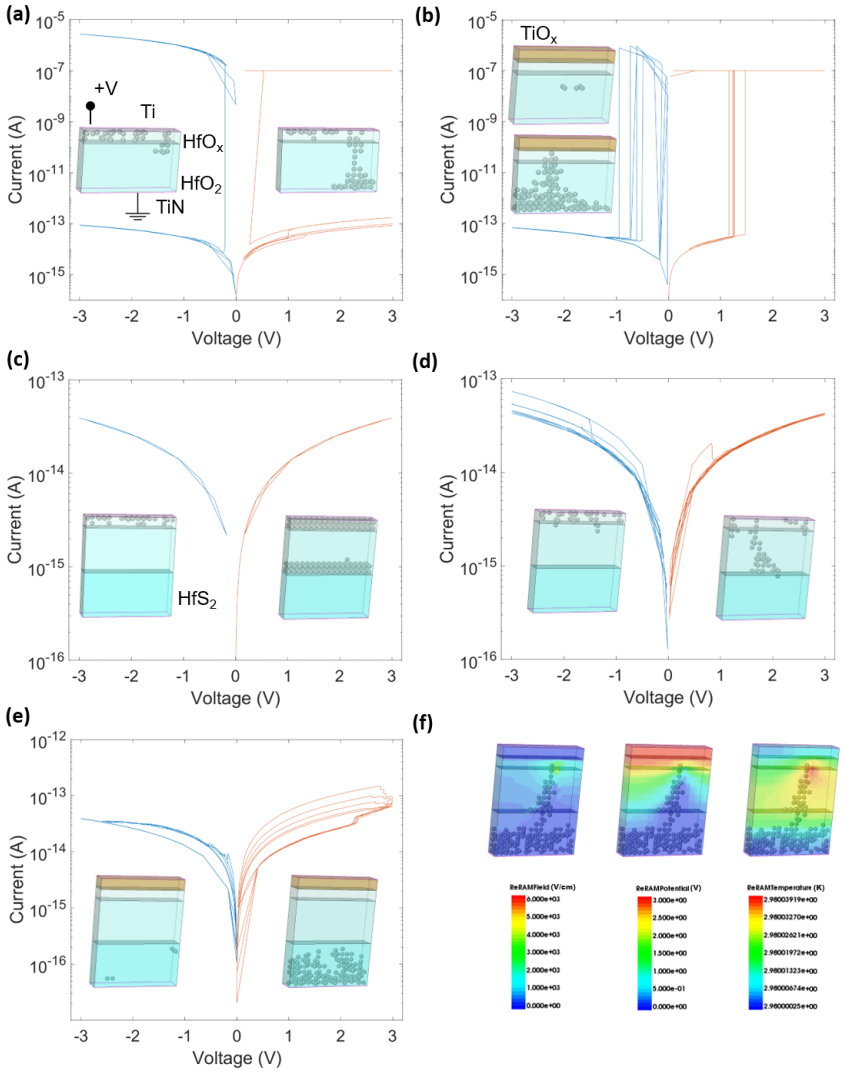

Figure 4: (a) Without the TiO_x region, only breakdown occurs in the HfO_x/ HfO_2 device. (b) With TiO_x, abrupt resistive switching is observed. (c) Without TiO_x but with HfS_2, we see only leakage current with no hysteresis (note, particles shown only in this subfigure are mobile vacancies in HfO_x during RESET, then oxygen ions in HfO_x and vacancies on the HfO_2/ HfS_2 interface during SET. (d) Allowing filament growth and recession in HfS_2 enables hysteretic behaviour but with poor filament stability. (e) Gradual and consistent resistive switching can be observed when adding TiO_x, replicating the structure of our devices. (f) Electric field, electrostatic potential and temperature variation in device as a result of filament growth.

Omitting the TiO_x region (Fig. 4a) provides no method for creating an imbalance between oxygen vacancies and ions in the switching layer of the device. This results in dielectric breakdown and vacancy filament formation, but prevents resistive switching using this biasing scheme.

Including the TiO_x region thus enables stable and repeatable resistive switching (Fig. 4b). By sequentially adding HfS_2 and allowing vacancy diffusion throughout the device (Fig. 4c), enabling stabilisation of mobile vacancies by transitioning to immobile vacancies/ filament formation (Fig. 4d) and finally adding TiO_x (Fig. 4e), the IV characteristics of our experimental devices can be replicated. Electric field, electrostatic potential and temperature variation in our device during filament growth are shown in a scenario where filament formation occurs almost from bottom to top electrode (Fig. 4f). However they represent an area for improvement as the reported n-type conductivity of the conductive filament in hafnia as reported in other work[12] has not been replicated.

4.1 Area Scaling

We show that by extrapolation of 3 data points for the same device as Fig. 4e, when scaling by area, a similar current exhibited by our experimental devices can be achieved (main text, Fig. 4a) Further data points were not taken as increasing the device cross sectional area beyond 8x8nm^2 presented a significant cost to simulation time (Fig. 5.)

Device width (nm)	Device length (nm)	Cross sectional area (nm²)	I @ 1V (A)	Measurement
1.5	8	12	2.40E-14	Simulation
8	8	64	7.00E-14	Simulation
30	30	900	9.00E-13	Simulation
5000	5000	25000000	2.50E-08	Extrapolated

Figure 5: Extrapolated from 3 simulations of the same device with different cross sectional areas, we can see that the current through the device at 1V in simulation is more similar to our experimental devices. This presents a possibility for reducing currents (and therefore energy consumption) in the device by scaling electrode size down.

4.2 HfS_2 Thickness Scaling

By investigating devices identical to Fig. 4e but with a HfS_2 region of variable thickness (Fig. 6a), we show that an increase of 3nm in HfS_2 thickness can decrease the peak conductance of the device by 3.5X (Fig. 6b).

This has been observed in our experimental devices where HfS_2 flakes of different thicknesses have been used to fabricate otherwise identical devices, supporting the idea of the HfS_2 region acting to limit currents and drive the gradual, compliance-free and forming-free resistive switching we have observed.

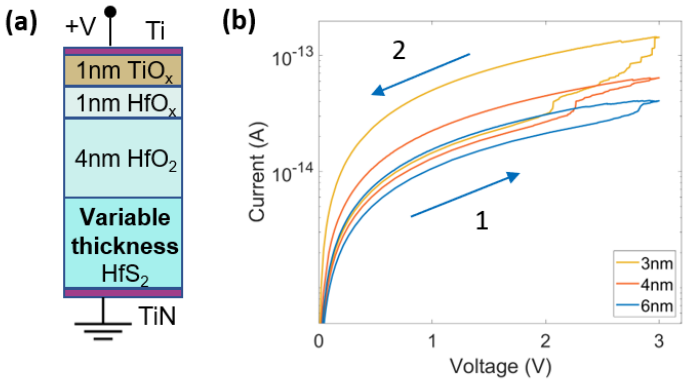

Figure 6: (a) Device structure with variable HfS_2 thickness. (b) Representative IV SET sweeps from otherwise identical devices with 3nm, 4nm and 6nm thick HfS_2 layers, showing decreased conductance and peak currents for devices with thicker HfS_2.

5 Description of Additional Supplementary Files

5.1 Supplementary Movie 1

Synchronised IV characteristics of a $Ti/TiO_x/HfO_x/HfO_2/TiN$ memristor showing abrupt, filamentary resistive switching due to charged oxygen vacancy generation and diffusion under applied field (spheres in the device structure). The charged, mobile oxygen vacancies transition to uncharged, immobile oxygen vacancies and form a filament bridging the top and bottom electrodes, creating a conductive pathway. A compliance is applied in the simulation to prevent complete dielectric breakdown. Bipolar resistive switching is demonstrated as oxygen ions diffuse and recombine with oxygen vacancies (not visualised for clarity) under applied field of opposite polarity.

5.2 Supplementary Movie 2

Synchronised IV characteristics of a $Ti/TiO_x/HfO_x/HfO_2/HfS_2/TiN$ memristor showing gradual resistive switching due to mobile, charged oxygen vacancy generation and diffusion under applied field (spheres in the device structure). The charged, mobile oxygen vacancies accumulate in the HfS_2 region resulting in a gradual modulation of the conductance of the device, but they do not form an electrode-bridging filament as in Supplementary Movie 1. Bipolar resistive switching is demonstrated as oxygen ions diffuse and recombine with oxygen vacancies (not visualised for clarity) under applied field of opposite polarity.

References

[1] YY Wang, SM Huang, K Yu, J Jiang, Y Liang, B Zhong, H Zhang, GF Kan, SF Quan, and J Yu. Atomically flat hfo2 layer fabricated by mild oxidation hfs2 with controlled number of layers. *Journal of Applied Physics*, 127(21), 2020.

[2] Tengyu Jin, Yue Zheng, Jing Gao, Yanan Wang, Enlong Li, Huipeng Chen, Xuan Pan, Ming Lin, and Wei Chen. Controlling native oxidation of hfs2 for 2d materials based flash memory and artificial synapse. *ACS Applied Materials & Interfaces*, 13(8):10639–10649, 2021.

[3] Irina Chircă, AbdulAziz AlMutairi, Barat Achinuq, Rongsheng Cai, Sarah Haigh, and Stephan Hofmann. Versatile fitting approach for operando spectroscopic imaging ellipsometry of hfs2 oxidation. *2D Materials*, 2024.

[4] Inc. Software Spectra. Optical data from sopra sa, 2023.

[5] Vinod K Sangwan, Hong-Sub Lee, Hadallia Bergeron, Itamar Balla, Megan E Beck, Kan-Sheng Chen, and Mark C Hersam. Multi-terminal memtransistors from polycrystalline monolayer molybdenum disulfide. *Nature*, 554(7693):500–504, 2018.

[6] Zhen-Xun Tang, Wen-Wei Tang, Xin-Gui Tang, Qiu-Xiang Liu, Yan-Ping Jiang, Wen-Hua Li, Zhen-Hua Tang, Xiao-Bin Guo, and Zhen-Fang Tang. Analog-type resistive switching behavior of au/hfo2/zno memristor fabricated on flexible mica substrate. *Physica E: Low-Dimensional Systems and Nanostructures*, 120:114047, 2020.

[7] Da Li, Bin Wu, Xiaojian Zhu, Juntong Wang, Byunghoon Ryu, Wei D Lu, Wei Lu, and Xiaogan Liang. Mos2 memristors exhibiting variable switching characteristics toward biorealistic synaptic emulation. *ACS nano*, 12(9):9240–9252, 2018.

[8] Hao Li, Li Tao, and Jian-Bin Xu. Intrinsic memristive mechanisms in 2d layered materials for high-performance memory. *Journal of Applied Physics*, 129(5), 2021.

[9] Marco A Villena, Fei Hui, Xianhu Liang, Yuanyuan Shi, Bin Yuan, Xu Jing, Kaichen Zhu, Shaochuan Chen, and Mario Lanza. Variability of metal/h-bn/metal memristors grown via chemical vapor deposition on different materials. *Microelectronics Reliability*, 102:113410, 2019.

[10] Chengbin Pan, Yanfeng Ji, Na Xiao, Fei Hui, Kechao Tang, Yuzheng Guo, Xiaoming Xie, Francesco M Puglisi, Luca Larcher, Enrique Miranda, et al. Coexistence of grain-boundaries-assisted bipolar and threshold resistive switching in multilayer hexagonal boron nitride. *Advanced functional materials*, 27(10):1604811, 2017.

[11] SS Teja Nibhanupudi, Anupam Roy, Dmitry Veksler, Matthew Coupin, Kevin C Matthews, Matthew Disiena, Ansh, Jatin V Singh, Ioana R Gearba-Dolocan, Jamie Warner, et al. Ultra-fast switching memristors based on two-dimensional materials. *Nature Communications*, 15(1):2334, 2024.

[12] Andre Zeumault, Shamiul Alam, Zack Wood, Ryan J Weiss, Ahmedullah Aziz, and Garrett S Rose. Tcad modeling of resistive-switching of hfo2 memristors: Efficient device-circuit co-design for neuromorphic systems. *Frontiers in Nanotechnology*, 3:734121, 2021.